Review of Scientific Instruments

RESEARCH ARTICLE | JANUARY 02 2024

Time-resolved ARPES with probe energy of 6.0/7.2 eV and switchable resolution configuration

Mojun Pan ; Junde Liu ; Famin Chen ; Ji Wang ; Chenxia Yun ; Tian Qian

Rev. Sci. Instrum. 95, 013001 (2024)
https://doi.org/10.1063/5.0177361

Review of Scientific Instruments ARTICLE pubs.aip.org/aip/rsi

Time-resolved ARPES with probe energy of 6.0/7.2 eV and switchable resolution configuration

Cite as: Rev. Sci. Instrum. 95, 013001 (2024); doi: 10.1063/5.0177361
Submitted: 21 September 2023 • Accepted: 9 December 2023 •
Published Online: 2 January 2024

Mojun Pan,[1,2] Junde Liu,[1,2] Famin Chen,[3] Ji Wang,[1,4] Chenxia Yun,[1,a)] and Tian Qian[1,a)]

AFFILIATIONS

[1] Beijing National Laboratory for Condensed Matter Physics and Institute of Physics, Chinese Academy of Sciences, Beijing 100190, China
[2] University of Chinese Academy of Sciences, Beijing 100049, China
[3] Southern University of Science and Technology, Shenzhen 518055, China
[4] Songshan Lake Materials Laboratory, Dongguan 523808, China

[a)] **Authors to whom correspondence should be addressed:** cxyun@iphy.ac.cn and tqian@iphy.ac.cn

ABSTRACT

We present a detailed exposition of the design for time- and angle-resolved photoemission spectroscopy using a UV probe laser source that combines the nonlinear effects of β-BaB_2O_4 and $KBe_2BO_3F_2$ optical crystals. The photon energy of the probe laser can be switched between 6.0 and 7.2 eV, with the flexibility to operate each photon energy setting under two distinct resolution configurations. Under the fully optimized energy resolution configuration, we achieve an energy resolution of 8.5 meV at 6.0 eV and 10 meV at 7.2 eV. Alternatively, switching to the other configuration enhances the temporal resolution, yielding a temporal resolution of 72 fs for 6.0 eV and 185 fs for 7.2 eV. We validated the performance and reliability of our system by applying it to measuring two typical materials: the topological insulator $MnBi_2Te_4$ and the excitonic insulator candidate Ta_2NiSe_5.

I. INTRODUCTION

Time- and angle-resolved photoemission spectroscopy (Tr-ARPES) is a cutting-edge technique that has been developed in the past decade. By combining ultrafast laser techniques with angle-resolved photoemission spectroscopy, Tr-ARPES provides a unique capability of investigating non-equilibrium band structures and photo-induced phase transitions in solid-state systems. Its remarkable capabilities have generated significant interest among researchers and have extensively been applied in the investigation of various quantum materials, including topological materials,[1–5] high-T_c superconductors,[6] excitonic insulators,[7,8] charge-density-wave systems,[9–11] Floquet band engineering,[12–14] and others.[15,16]

Over the past few decades, several Tr-ARPES instruments with diverse designs and configurations have been developed.[17–24] The majority of these instruments aim to develop suitable probe laser sources through the utilization of high harmonics generation (HHG) in noble gases[20–24] or second-order nonlinear optical effects in optical crystals.[17–19] The probe beam generated by HHG offers advantages such as a higher photon energy (>20 eV), a wide range of tunable wavelengths,[25] and an enhanced temporal resolution. On the other hand, instruments that employ optical nonlinear crystals for probe laser generation are more widely accessible and generally provide a superior energy resolution.

Fourth harmonic generation (FHG) in β-BaB_2O_4 (BBO) is a widely utilized technique for generating probe lasers, resulting in a photon energy of ~6.0 eV. By coupling the $KBe_2BO_3F_2$ (KBBF) crystal[26,27] with the prism technique, ultraviolet (UV) lasers with a higher photon energy can be generated. Yang *et al.*[17] developed a probe photon energy of 6.7 eV with a temporal resolution of ~1 ps, while Bao *et al.*[18] developed a tunable probe photon energy range of 5.9–7.0 eV, with the temporal resolution improved to 320 fs at 7.0 eV.

In this study, we developed a UV laser source with a photon energy of 7.2 eV and fully optimized temporal resolution of 185 fs. Notably, we have also incorporated a versatile design that facilitates

convenient switching between 6.0/7.2 eV and different resolution configurations. This setup can be operated with energy resolutions of 8.7 meV for 6.0 eV and 10 meV for 7.2 eV, which is particularly advantageous for accurately probing fine features of electronic band structures. Furthermore, it can be easily reconfigured to achieve improved temporal resolutions of 72 fs for 6.0 eV and 185 fs for 7.2 eV, which are highly beneficial for investigating transient non-equilibrium processes. The combination of a two-color UV laser source with our compatibility design substantially enhances experimental efficiency. To demonstrate the performance of our setup, we conducted measurements on several materials, including topological insulators Bi_2Se_3[28,29] and $MnBi_2Te_4$[30] and the excitonic insulator candidate Ta_2NiSe_5.[31–33]

II. EXPERIMENTAL SETUP

A. Tr-ARPES layout

Figure 1 presents a schematic overview of our Tr-ARPES system. The system employs a Yb-doped fiber laser as the fundamental beam (FB) with a central wavelength of 1030 nm ($h\nu = 1.2$ eV). The FB provides an adjustable output repetition rate ranging from 1 Hz to 1 MHz, accompanied by a pulse duration of 200 fs and a maximum pulse energy of 150 μJ (when operating at or below 300 kHz).

The FB passes through a setup comprising a half-wave plate and thin film polarizer (TFP), allowing for an adjustable splitting power ratio. The beam transmitted through the TFP subsequently enters the multipass cell (MPC) compressor for secondary compression, which reduces the duration to 75 fs. The compressed beam (CB) is then combined with the uncompressed beam that is reflected by the TFP. In experiments, the CB with a pulse duration of 75 fs can be utilized to enhance the temporal resolution or the FB with a pulse duration of 200 fs can be utilized to enhance the energy resolution.

The beam is then divided by a half-wave plate and TFP before entering the main optical path. This division serves two main purposes: First, power reduction, since the total power requirements for the system are not substantial; this reduction helps counteract the system instability caused by thermal effects. Second, the high-power beam that is reflected can be employed as a dual time-delayed pump with a high power density, customized to meet specific experimental requirements.

After entering the main optical path, the beam is focused by a concave mirror onto a BBO crystal ($\theta = 23°$) with a thickness of 0.5 mm, inducing second harmonic (SH) generation at 515 nm ($h\nu = 2.4$ eV). Subsequent to this setup, the residual 1030 nm beam is temporally and spatially aligned with the 515 nm beam precisely. These two beams are then directed onto a BBO crystal ($\theta = 32.5°$) with a thickness of 0.15 mm, resulting in the production of a third harmonic (TH) generation at 343 nm ($h\nu = 3.6$ eV). The efficiency of generating the 343 nm signal can achieve around 30% under the FB and 18% under the CB.

The 343, 515, and 1030 nm signals produced can be effectively monochromatized, yielding a three-way beam consisting of distinct monochromatic components. The 515 and 343 nm signals are divided using a beam splitter, while a fraction of the 343 nm signal is directed onto a KBBF crystal to produce a 171 nm ($h\nu = 7.2$ eV) signal. The residual 343 and 515 nm signals are then focused on a BBO crystal ($\theta = 77°$) with a thickness of 0.1 mm after temporal and spatial alignments, generating a probe beam at 206 nm ($h\nu = 6$ eV).

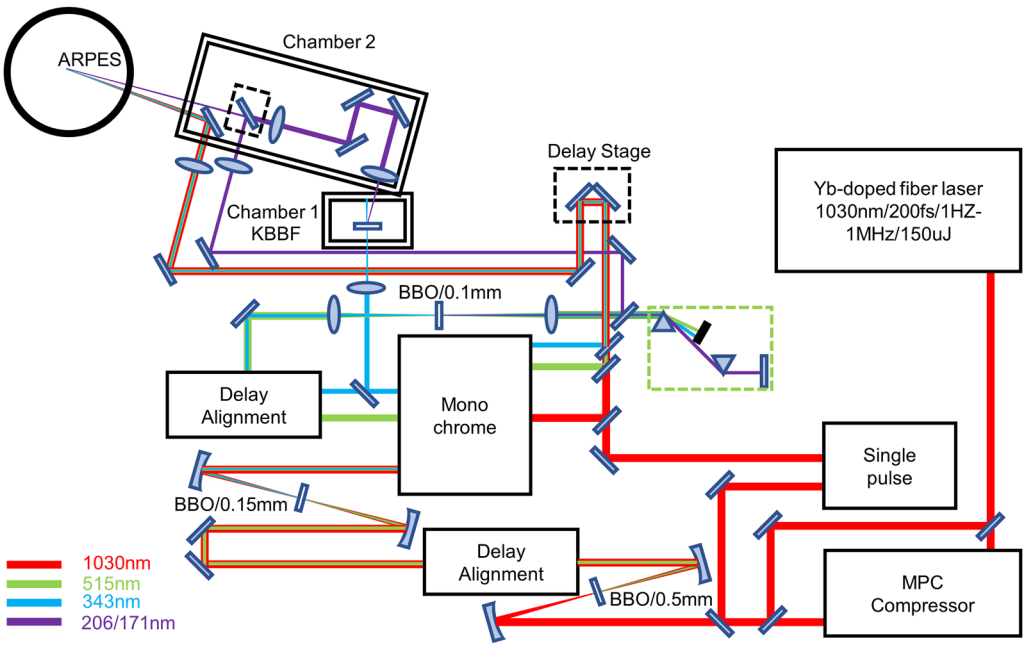

FIG. 1. Schematic diagram of Tr-ARPES with probe photon energies at 6.0 and 7.2 eV and pump photon energies at 1.2, 2.4, and 3.6 eV.

The surplus portions of the 515 and 343 nm signals, along with the additional 1030 nm signal, are combined and directed through a hollow retroreflector (Newport UBBR1-1S) positioned on a delay stage. The merged beam is subsequently focused onto the sample, serving as the pump with variable photon energies. To mitigate pump power, a rotating attenuator is placed in front of the chamber.

To attain a resolution approaching the Fourier limit ($\Delta E * \Delta T \approx 1800$ fs meV), the 206 nm signal is subjected to dispersion compensation and is subsequently monochromatized using a pair of prisms before entering the chamber. Conversely, for the probe beam of 171 nm, a pre-compensation scheme is utilized to alleviate the dispersion effects induced by the 343 nm signal, owing to the challenges associated with direct dispersion compensation.

Our ARPES system is equipped with the following components: (1) a hemispherical analyzer (Scienta Omicron DA30-L), (2) a helium lamp system (Scienta Omicron VUV5050) with photon energies of 21.2 and 40.8 eV, offering an energy resolution of less than 5 meV, (3) a six-axis sample manipulator (Fermion instrument) capable of operating at temperatures as low as 6 K, (4) an annealing chamber featuring an Argon gun (SPECS), with radiation capability (up to 700 °C) and laser heating capacity (up to 1200 °C), enabling fundamental sample processing, and (5) our internally developed Delay Stage software, seamlessly integrated with the analyzer software SES, facilitating automated spectrum sweeping at different delay times. Moreover, our main ARPES chamber achieves an exceptional vacuum level, surpassing even 3×10^{-11} Torr following baking procedures.

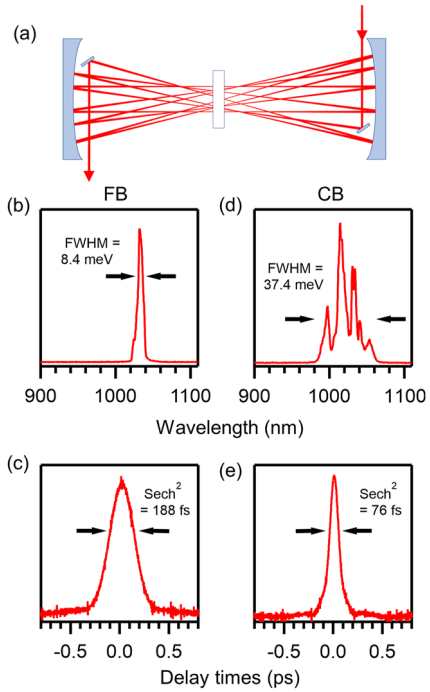

FIG. 2. MPC (multi-pass cell) diagram and spectra/duration results. (a) MPC diagram. [(b) and (c)] Spectra and duration of FB (fundamental beam) before MPC. [(d) and (e)] Spectra and duration of CB (compressed beam) after MPC.

B. MPC pulse compress

The pulse duration of a UV laser is commonly influenced by the pulse duration of the incident beam. Employing a shorter pulse duration enhances the temporal resolution of Tr-ARPES. Additionally, the reduced pulse duration enables a higher peak power density for the pump, thereby facilitating processes such as optical modulation and photo-induced phase transitions. As a result, we employ secondary compression techniques to achieve a shorter pulse duration.

When there is no dispersion, the product of the spectral width and the duration of the pulse remains constant, which implies that shorter laser pulses have a broader spectral width. Thus, in order to achieve shorter laser pulses, it is necessary to broaden the pulse spectrum to encompass the desired pulse duration. Nonlinear self-phase modulation within a nonlinear medium is a commonly employed method for achieving spectral broadening. Among the various techniques for pulse width compression, hollow fiber compression and MPC compression[34,35] have emerged as the most widely adopted strategies globally. Comparatively, the MPC scheme offers several advantages over the hollow fiber compression scheme, including a high efficiency, a compact footprint, and an enhanced stability. Consequently, we selected the MPC compression scheme and have successfully reduced the pulse duration from 200 to 75 fs, achieving an efficiency that exceeds 80%.

Figure 2(a) illustrates the optical path of the MPC. A 10W FB laser with a duration of 200 fs at a repetition rate of 500 kHz is directed onto the MPC through a D-shaped reflection mirror. The MPC system is comprised of two 2-in. concave mirrors, each with a focal length of 250 mm. Positioned between these mirrors are a fused silica element with a thickness of 3 mm and an element coated with a double-sided permeability-enhancing film of 1030 nm.

During its course through the MPC, the beam undergoes 36 reflections, with 18 beam drop-off points on the mirrors arranged in a circular pattern. Following these reflections, the spectrally broadened beam exits through another D-shaped reflection mirror. Passing through the fused silica element in each round introduces 100 fs^2 of group delay dispersion (GDD), resulting in an accumulated dispersion of ~3600 fs^2. Furthermore, the MPC itself contributes a certain level of positive dispersion. To counteract this and the dispersion arising from the broadened spectrum, chirped mirrors are employed. These mirrors have a combined dispersion value of −5000 fs^2. The compression capabilities of an individual MPC exhibit limitations. To attain further pulse duration compression, an additional round of MPC compression can be executed. Following dispersion compensation, we achieve a CB power of 8 W with an efficiency of 80%. Figures 2(b)–2(e) present the spectral composition before and after compression, along with the ensuing alteration in the pulse duration.

C. Character of the pump and probe

Figure 3 illustrates the spectra and cross correlation results of 515 and 343 nm before [(a), (b), (e), and (f)] and after [(c), (d), (g), and (h)] compression.

To calibrate the spot size of the pump pulses on the analyzer focus, we measured the pump power behind the sample position

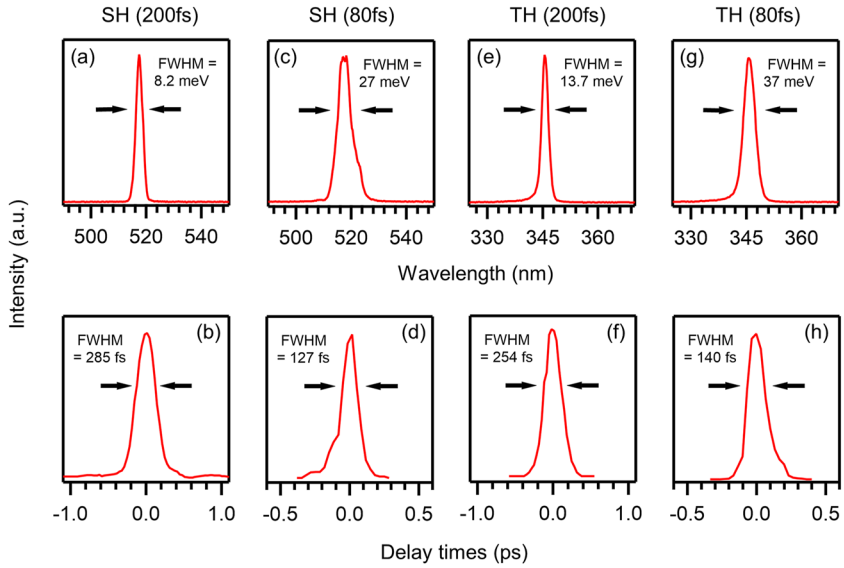

FIG. 3. Spectra and cross correlation data for SH (second harmonic) with center wavelength at 515 nm [(a)–(d)] and TH (third harmonic) with center wavelength at 343 nm [(e)–(h)] before and after MPC pulse compression.

by scanning the spot along the sharp edge of the gold (Au) sample. The Gaussian curve can be derived through the differentiation of this power curve, with the full width at half maximum (FWHM) of the Gaussian curve representing the size of the pump laser. Since measuring the probe intensity behind the sample is unfeasible, we choose to use the curve that illustrates the intensity changes of the counts on the analyzer as the sample position is adjusted. This measurement was carried out with the sample surface placed at a 45° angle to the incident laser. Figure 4 illustrates a spot size of 6 eV, which is ~46 × 25 μm^2. After compensating for the lateral spread resulting from the 45° incidence angle, the spot size is ~32 × 25 μm^2. Further details regarding the spot size of the remaining pump and probe are presented in Table I.

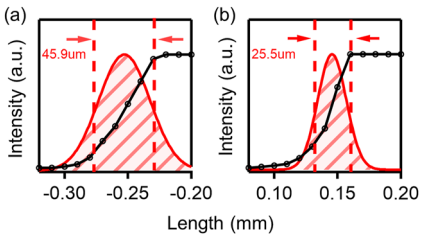

FIG. 4. Spot size at 6 eV with a 45° incidence angle. (a) Horizontal spot size. (b) Vertical spot size.

TABLE I. Spot size of the pump and probe.

hν (eV)	Horizon (μm)	Vertical (μm)
1.2	107.2	64.3
2.4	75.5	61.3
3.6	45.4	88
6	45.9	25.5
7.2	23.0	22.56

III. ENERGY RESOLUTION AND TEMPORAL RESOLUTION

The energy resolution is obtained through the measurement of the Fermi edge of the polycrystalline gold at 10 K. This measurement entails fitting a convolution of a Gaussian distribution $g(\omega) = e^{(-4\ln 2)\omega^2/R_e^2}$ and the Fermi–Dirac distribution $f(\omega) = 1/\left(e^{\hbar\omega/k_BT} + 1\right)$ to the data, where the FWHM of the Gaussian distribution characterizes the energy resolution. The temporal resolution measurement involves fitting the temporal distribution curve of the density of states in the high-energy region of an HOPG sample. The fitting function is the product of the Heaviside function and a single-exponential function convolved with a Gaussian function,[36]

$$I(t) = A\left(1 + \mathrm{erf}\left(\frac{t - t_0}{\Delta t}\right)\right)e^{-\frac{t-t_0}{\tau}} + B.$$

Here, the parameter Δt corresponds to the temporal resolution, while τ corresponds to the relaxation time of decay.

Figure 5 illustrates the energy and temporal resolution curves for the 2.4 eV pump with both 80 and 200 fs beams. Table II presents the values for the temporal and energy resolutions across varying pump photon energies. During excitation, the temporal resolution with a 1.2 eV pump is slightly worse than that with a 2.4 eV pump. This difference can be attributed to the broader pulse duration of the 1.2 eV pump in comparison with the 2.4 eV pump.

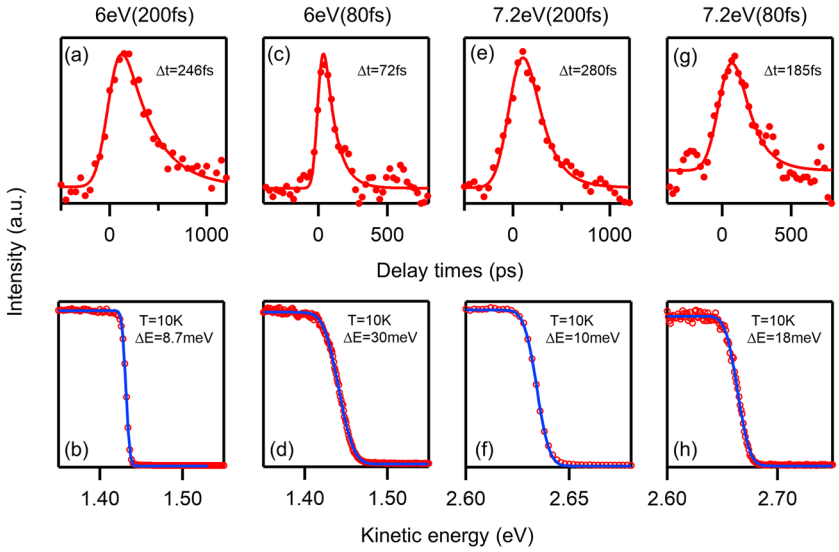

FIG. 5. Energy and temporal resolutions undervarious configurations. The energy resolution is determined for polycrystalline gold at a temperature of 10 K, while the temporal resolution is evaluated using a 2.4 eV pump. [(a)–(d)] Raw and fitted data illustrating time and energy resolutions of 6 eV at 200 and 80 fs. [(e)–(h)] Raw and fitted data demonstrating temporal and energy resolutions of 7.2 eV at 200 and 80 fs.

TABLE II. Different resolutions under-various configurations.

	Δt 1.2 eV (fs)	Δt 2.4 eV (fs)	ΔE (meV)
6 eV(80 fs)	95	72	30
7.2 eV(80 fs)	195	185	18
6 eV(200 fs)	290	246	8.7
7.2 eV(200 fs)	300	280	10

IV. MEASUREMENT

A. Equilibrium state of Bi_2Se_3

Figure 6 depicts the measurement of the equilibrium state of Bi_2Se_3 at the Γ-point using photon energies of 6 and 7.2 eV at a temperature of 10 K. Owing to the higher photon energy of 7.2 eV, a larger momentum space can be observed within the same acceptance angle range. According to the formula $k_{\parallel} = \sqrt{2mE_{kin}}\sin\theta/\hbar$, the maximum observable momentum k at 7.2 eV is 0.84 (1/Å), with a momentum k of 0.22 (1/Å) at a 15° angle. For 6 eV, the maximum observable momentum k is 0.62 (1/Å), with a momentum k of 0.16 (1/Å) at a 15° angle. With an equal number of analyzer channels, 6 eV provides an improved angular resolution. Furthermore, since measurements at 6 and 7.2 eV capture distinct kz values, it becomes feasible to investigate band dispersion at diverse kz values in specific materials.[37]

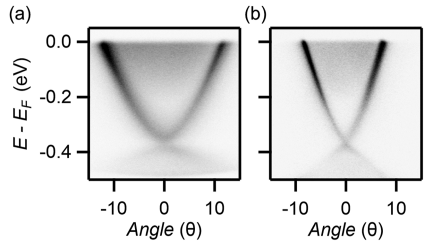

FIG. 6. Depiction of equilibrium state of Bi_2Se_3 in Tr-ARPES. (a) Band structure of Bi_2Se_3 at the Γ point measured by 6 eV. (b) Band structure of Bi_2Se_3 at the Γ point measured by 7.2 eV.

B. Measurement of the gap in $MnBi_2Te_4$

To validate the energy resolution capability of our equipment, we chose the topological material $MnBi_2Te_4$ for testing. Previous research has indicated the existence of a gap in the topological surface state of $MnBi_2Te_4$, with an approximate gap size of 10 meV.[30] We conducted band structure measurements at the Γ-point of $MnBi_2Te_4$ by employing the 7.2 eV probe laser with a configuration of optimized energy resolution at 10 meV. Figure 7(a) illustrates the spectrum with a 2D intensity contour map at an energy 0.2 eV below the Fermi level. Figure 7(b) presents the band structure results at the Γ-point along with the corresponding tangent in Fig. 7(a), while Fig. 7(c) presents the second derivative in the energy direction of the data. We performed an analysis of individual energy distribution curves (EDCs) at various momentum k values, as shown in Fig. 7(d). The arrows in the figure indicate the peak positions of the EDCs at different momenta, corresponding to the gap size. Through the examination of these peak positions, we confirmed that the gap at the Γ-point is around 10 meV, thus validating the energy resolution capability of our equipment.

C. Dynamic of Ta_2NiSe_5

We selected the excitonic insulator candidate Ta_2NiSe_5 to validate the temporal resolution capabilities of our experimental setup.

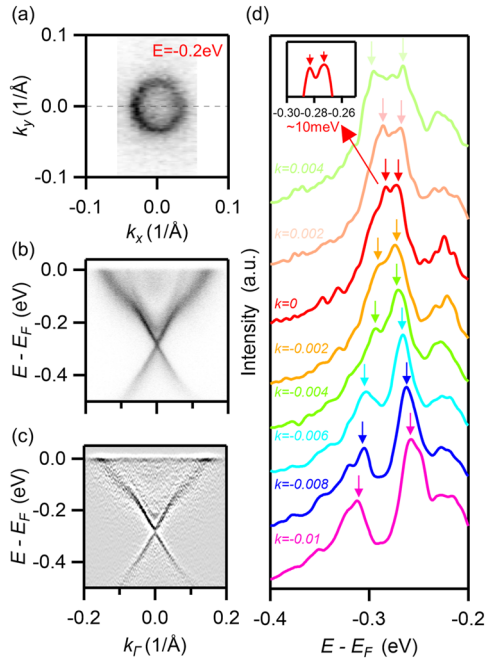

FIG. 7. Measurement results of $MnBi_2Te_4$ with the configuration of a better energy resolution. (a) Spectrum with the 2D intensity contour map at an energy 0.2 eV below the Fermi level. (b) Band structure at the Γ-point along with the corresponding tangent in panel (a). (c) Second derivative in the energy direction of panel (b). (d) Energy distribution curves (EDCs) at different k points from panel (b), with peak positions indicated by arrows.

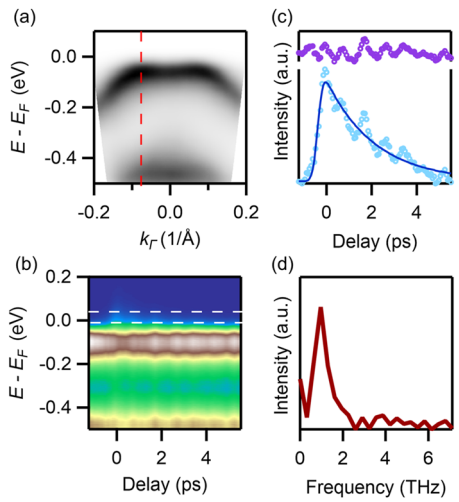

FIG. 8. Measurement results of Ta_2NiSe_5. (a) Band structure at the Γ point.(b) Photoemission intensity as a function of energy and time delay at the red dashed line cut in panel (a). (c) Bottom: The integrated intensity as a function of time delay at the region of the white dashed line in panel (b). The blue curve indicates the incoherent part fitted by the product of the Heaviside function and a single-exponential function convolved with a Gaussian function. Top: Intensity after removing the incoherent part. (d) The corresponding Fourier transform magnitude of the curve in the top of panel (c).

In this material, a hole-like pocket exists at the center of the Brillouin zone and a gap opens below the transition temperature.[31–33] In Fig. 8(a), we present the static band structure of the hole band at the Γ-point measured by a 6 eV probe laser with an optimized temporal resolution. Upon excitation with a 1.2 eV pump laser at a fluence of 0.25 mJ/cm^2, Fig. 8(b) illustrates the photoemission intensity as a function of energy and time delay along the red dashed line in panel (a). The temporal evolution of the integrated intensity is shown in the lower part of Fig. 8(c), corresponding to the region outlined by the white dashed line in panel (b). The fitted blue solid curve represents the incoherent component within the data, modeled as the product of the Heaviside function and a single-exponential function convolved with a Gaussian function. After subtracting the incoherent contribution, the upper part of Fig. 8(c) shows a clear oscillation. Through Fourier transformation, we determined a frequency of ~1.0 THz, consistent with the A_g phonon mode.[7,38] It is worth noting that some higher-frequency oscillations have not been observed here, which may be due to limitations in the current temporal resolution. This result highlights the capability of our apparatus to capture fast dynamic phenomena within materials, encompassing collective mode oscillations and rapid interaction processes.

V. CONCLUSION

In summary, we have successfully developed a time-resolved ARPES system employing a 200 fs Yb-doped laser coupled with a hemispherical energy analyzer. The photon energy of the pump laser can be selectively tuned to 1.2, 2.4, and 3.6 eV, while the photon energy of the probe laser is adjustable to 6 and 7.2 eV. Through the application of MPC compression to the laser, we have achieved a 75 fs CB. The use of the 200 fs FB configuration has notably improved the energy resolution, and alternatively, employing the 80 fs CB configuration has provided remarkable enhancements in the temporal resolution. The enhanced energy resolution allows us to discern intricate features within specific band structures, as evidenced by our successful verification of a gap size of ~10 meV in the surface state of the topological material $MnBi_2Te_4$. Moreover, the improved temporal resolution empowers us to explore material dynamics, as evidenced by our successful characterization of oscillations in Ta_2NiSe_5. Our innovative system presents an adaptable platform for future experiments, readily customizable to meet diverse research requirements.

ACKNOWLEDGMENTS

We thank H. C. Lei and S. J. Tian from Renmin University (Beijing) for providing high quality $MnBi_2Te_4$ samples, Z. W. Wang from Beijing Institute of Technology for providing Ta_2NiSe_5 samples, and S. Y. Xu from Northwest University (Xi'an, Shaanxi) for providing optical guidance.

This work was supported by the Ministry of Science and Technology of China (Grant No. 2022YFA1403800), the National Natural Science Foundation of China (Grant Nos. U1832202, 22A6005, and 11888101), the Beijing Municipal Science and Technology Commission (Grant No. Z171100002017018), the Chinese Academy of Sciences (Grant Nos. XDB33000000 and XDB28000000), the Informatization Plan of Chinese Academy of Sciences (Grant No. CAS-WX2021SF-0102), and the Synergetic Extreme Condition User Facility (SECUF).

AUTHOR DECLARATIONS

Conflict of Interest

The authors have no conflicts to disclose.

Author Contributions

Mojun Pan, Junde Liu, and Famin Chen contributed equally to this work.

Mojun Pan: Data curation (equal); Investigation (equal); Software (equal); Writing – original draft (equal); Writing – review & editing (equal). **Junde Liu**: Data curation (equal); Investigation (equal); Writing – original draft (equal); Writing – review & editing (equal). **Famin Chen**: Investigation (equal); Software (equal); Writing – original draft (equal). **Ji Wang**: Investigation (supporting). **Chenxia Yun**: Conceptualization (equal); Project administration (equal); Supervision (equal). **Tian Qian**: Conceptualization (equal); Project administration (equal); Supervision (equal); Writing – review & editing (equal).

DATA AVAILABILITY

The data that support the findings of this study are available from the corresponding author upon reasonable request.

REFERENCES

[1] Y. Wang, D. Hsieh, E. Sie, H. Steinberg, D. Gardner, Y. Lee, P. Jarillo-Herrero, and N. Gedik, Phys. Rev. Lett. **109**, 127401 (2012).
[2] J. A. Sobota, S. Yang, J. G. Analytis, Y. Chen, I. R. Fisher, P. S. Kirchmann, and Z.-X. Shen, Phys. Rev. Lett. **108**, 117403 (2012).
[3] J. Sánchez-Barriga, E. Golias, A. Varykhalov, J. Braun, L. Yashina, R. Schumann, J. Minár, H. Ebert, O. Kornilov, and O. Rader, Phys. Rev. B **93**, 155426 (2016).
[4] S. Ciocys, T. Morimoto, R. Mori, K. Gotlieb, Z. Hussain, J. G. Analytis, J. E. Moore, and A. Lanzara, Npj Quantum Mater. **5**, 16 (2020).
[5] J. A. Sobota, S.-L. Yang, D. Leuenberger, A. F. Kemper, J. G. Analytis, I. R. Fisher, P. S. Kirchmann, T. P. Devereaux, and Z.-X. Shen, J. Electron Spectrosc. Relat. Phenom. **195**, 249 (2014).
[6] L. Perfetti, P. Loukakos, M. Lisowski, U. Bovensiepen, H. Eisaki, and M. Wolf, Phys. Rev. Lett. **99**, 197001 (2007).
[7] T. Tang, H. Wang, S. Duan, Y. Yang, C. Huang, Y. Guo, D. Qian, and W. Zhang, Phys. Rev. B **101**, 235148 (2020).
[8] K. Okazaki, Y. Ogawa, T. Suzuki, T. Yamamoto, T. Someya, S. Michimae, M. Watanabe, Y. Lu, M. Nohara, H. Takagi, N. Katayama, H. Sawa, M. Fujisawa, T. Kanai, N. Ishii, J. Itatani, T. Mizokawa, and S. Shin, Nat. Commun. **9**, 4322 (2018).
[9] F. Schmitt, P. S. Kirchmann, U. Bovensiepen, R. G. Moore, L. Rettig, M. Krenz, J.-H. Chu, N. Ru, L. Perfetti, D. H. Lu, M. Wolf, I. R. Fisher, and Z.-X. Shen, Science **321**, 1649 (2008).
[10] J. C. Petersen, S. Kaiser, N. Dean, A. Simoncig, H. Y. Liu, A. L. Cavalieri, C. Cacho, I. C. E. Turcu, E. Springate, F. Frassetto, L. Poletto, S. S. Dhesi, H. Berger, and A. Cavalleri, Phys. Rev. Lett. **107**, 177402 (2011).
[11] T. Rohwer, S. Hellmann, M. Wiesenmayer, C. Sohrt, A. Stange, B. Slomski, A. Carr, Y. Liu, L. M. Avila, M. Kalläne, S. Mathias, L. Kipp, K. Rossnagel, and M. Bauer, Nature **471**, 490 (2011).
[12] Y. Wang, H. Steinberg, P. Jarillo-Herrero, and N. Gedik, Science **342**, 453 (2013).
[13] F. Mahmood, C.-K. Chan, Z. Alpichshev, D. Gardner, Y. Lee, P. A. Lee, and N. Gedik, Nat. Phys. **12**, 306 (2016).
[14] S. Zhou, C. Bao, B. Fan, H. Zhou, Q. Gao, H. Zhong, T. Lin, H. Liu, P. Yu, P. Tang, S. Meng, W. Duan, and S. Zhou, Nature **614**, 75 (2023).
[15] A. L. Cavalieri, N. Müller, T. Uphues, V. S. Yakovlev, A. Baltuška, B. Horvath, B. Schmidt, L. Blümel, R. Holzwarth, S. Hendel, M. Drescher, U. Kleineberg, P. M. Echenique, R. Kienberger, F. Krausz, and U. Heinzmann, Nature **449**, 1029 (2007).
[16] Z. Tao, C. Chen, T. Szilvási, M. Keller, M. Mavrikakis, H. Kapteyn, and M. Murnane, Science **353**, 62 (2016).
[17] Y. Yang, T. Tang, S. Duan, C. Zhou, D. Hao, and W. Zhang, Rev. Sci. Instrum. **90**, 063905 (2019).
[18] C. Bao, H. Zhong, S. Zhou, R. Feng, Y. Wang, and S. Zhou, Rev. Sci. Instrum. **93**, 013902 (2022).
[19] Y. Ishida, T. Otsu, A. Ozawa, K. Yaji, S. Tani, S. Shin, and Y. Kobayashi, Rev. Sci. Instrum. **87**, 123902 (2016).
[20] F. Chen, J. Wang, M. Pan, J. Liu, J. Huang, K. Zhao, C. Yun, T. Qian, Z. Wei, and H. Ding, Rev. Sci. Instrum. **94**, 043905 (2023).
[21] E. J. Sie, T. Rohwer, C. Lee, and N. Gedik, Nat. Commun. **10**, 3535 (2019).
[22] G. Rohde, A. Hendel, A. Stange, K. Hanff, L.-P. Oloff, L. Yang, K. Rossnagel, and M. Bauer, Rev. Sci. Instrum. **87**, 103102 (2016).
[23] M. Puppin, Y. Deng, C. W. Nicholson, J. Feldl, N. Schröter, H. Vita, P. Kirchmann, C. Monney, L. Rettig, M. Wolf, and R. Ernstorfer, Rev. Sci. Instrum. **90**, 023104 (2019).
[24] A. K. Mills, S. Zhdanovich, M. X. Na, F. Boschini, E. Razzoli, M. Michiardi, A. Sheyerman, M. Schneider, T. J. Hammond, V. Süss, C. Felser, A. Damascelli, and D. J. Jones, Rev. Sci. Instrum. **90**, 083001 (2019).
[25] J. Wang, F. Chen, M. Pan, S. Xu, R. Lv, J. Liu, Y. Li, S. Fang, Y. Chen, J. Zhu *et al.*, Opt. Express **31**, 9854 (2023).
[26] B. Wu, D. Tang, N. Ye, and C. Chen, Opt. Mater. **5**, 105 (1996).
[27] C. Chen, G. Wang, X. Wang, and Z. Xu, Appl. Phys. B **97**, 9 (2009).
[28] H. Zhang, C.-X. Liu, X.-L. Qi, X. Dai, Z. Fang, and S.-C. Zhang, Nat. Phys. **5**, 438 (2009).
[29] Y. Xia, D. Qian, D. Hsieh, L. Wray, A. Pal, H. Lin, A. Bansil, D. Grauer, Y. S. Hor, R. J. Cava, and M. Z. Hasan, Nat. Phys. **5**, 398 (2009).
[30] H. Li, S.-Y. Gao, S.-F. Duan, Y.-F. Xu, K.-J. Zhu, S.-J. Tian, J.-C. Gao, W.-H. Fan, Z.-C. Rao, J.-R. Huang, J.-J. Li, D.-Y. Yan, Z.-T. Liu, W.-L. Liu, Y.-B. Huang, Y.-L. Li, Y. Liu, G.-B. Zhang, P. Zhang, T. Kondo, S. Shin, H.-C. Lei, Y.-G. Shi, W.-T. Zhang, H.-M. Weng, T. Qian, and H. Ding, Phys. Rev. X **9**, 041039 (2019).
[31] Y. Wakisaka, T. Sudayama, K. Takubo, T. Mizokawa, M. Arita, H. Namatame, M. Taniguchi, N. Katayama, M. Nohara, and H. Takagi, Phys. Rev. Lett. **103**, 026402 (2009).
[32] S. Mor, M. Herzog, D. Golež, P. Werner, M. Eckstein, N. Katayama, M. Nohara, H. Takagi, T. Mizokawa, C. Monney, and J. Stähler, Phys. Rev. Lett. **119**, 086401 (2017).
[33] K. Fukutani, R. Stania, C. Il Kwon, J. S. Kim, K. J. Kong, J. Kim, and H. W. Yeom, Nat. Phys. **17**, 1024 (2021).
[34] L. Lavenu, M. Natile, F. Guichard, Y. Zaouter, X. Delen, M. Hanna, E. Mottay, and P. Georges, Opt. Lett. **43**, 2252 (2018).
[35] J. Weitenberg, T. Saule, J. Schulte, and P. Rußbüldt, IEEE J. Quantum Electron. **53**, 8600204 (2017).
[36] C. Bao, L. Luo, H. Zhang, S. Zhou, Z. Ren, and S. Zhou, Rev. Sci. Instrum. **92**, 033904 (2021).
[37] Y. Zhong, J. Liu, X. Wu, Z. Guguchia, J.-X. Yin, A. Mine, Y. Li, S. Najafzadeh, D. Das, C. Mielke III, R. Khasanov, H. Luetkens, T. Suzuki, K. Liu, X. Han, T. Kondo, J. Hu, S. Shin, Z. Wang, X. Shi, Y. Yao, and K. Okazaki, Nature **617**, 488 (2023).
[38] D. Werdehausen, T. Takayama, M. Höppner, G. Albrecht, A. W. Rost, Y. Lu, D. Manske, H. Takagi, and S. Kaiser, Sci. Adv. **4**, eaap8652 (2018).